

Optical polarimetric measurement of surface acoustic waves

Cite as: Appl. Phys. Lett. **119**, 181106 (2021); doi: [10.1063/5.0066362](https://doi.org/10.1063/5.0066362)

Submitted: 10 August 2021 · Accepted: 18 October 2021 ·

Published Online: 2 November 2021



View Online



Export Citation



CrossMark

K. Taga,^{1,a)} R. Hisatomi,^{2,3,a)} Y. Ohnuma,¹ R. Sasaki,⁴ T. Ono,^{2,5,6} Y. Nakamura,^{1,4} and K. Usami^{1,a)}

AFFILIATIONS

¹Research Center for Advanced Science and Technology (RCAST), The University of Tokyo, Meguro-ku, Tokyo 153-8904, Japan

²Institute for Chemical Research (ICR), Kyoto University, Gokasho, Uji, Kyoto 611-0011, Japan

³PRESTO, Japan Science and Technology Agency, Kawaguchi-shi, Saitama 332-0012, Japan

⁴RIKEN Center for Quantum Computing (RQC), RIKEN, Wako, Saitama 351-0198, Japan

⁵Center for Spintronics Research Network, Institute for Chemical Research, Kyoto University, Gokasho, Uji, Kyoto 611-0011, Japan

⁶Center for Spintronics Research Network, Graduate School of Engineering Science, Osaka University, Toyonaka, Osaka 560-0043, Japan

^{a)}Authors to whom correspondence should be addressed: taga@issp.u-tokyo.ac.jp; hisatomi.ryusuke.2a@kyoto-u.ac.jp; and usami@qc.rcast.u-tokyo.ac.jp

ABSTRACT

A surface acoustic wave (SAW) is utilized in diverse fields ranging from physics, engineering, to biology for transducing, sensing, and processing various signals. Optical measurement of the SAW provides valuable information since the amplitude and the phase of the displacement field can be measured locally with the resolution limited by the spot size of the optical beam. So far, optical measurement techniques rely on modulation of the optical path, phase, or diffraction associated with SAWs. Here, we demonstrate that SAWs can be measured with an optical polarimeter. We show that the slope of the periodically tilting surface due to the coherently driven SAW is translated into the angle of polarization rotation, which can be straightforwardly calibrated when polarimeters work in the shot-noise-limited regime. The polarimetric measurement of SAWs is, thus, beneficial for quantitative studies of SAW-based technologies.

Published under an exclusive license by AIP Publishing. <https://doi.org/10.1063/5.0066362>

A surface acoustic wave (SAW) is a Rayleigh wave propagating on the surface of elastic media for which the longitudinal and transverse components are intertwined.^{1,2} SAWs are ideally suited in transducing, sensing, and processing in a form of coherent phonons, where they can be efficiently and coherently excited and detected electronically through the piezoelectric effect using interdigitated transducers (IDTs). SAWs have thus been used in various electronic devices. SAW filters, for instance, can be ubiquitously found in cellular phones.^{3–5} SAW-based biosensors are now popular in detecting molecules in liquid media.^{6–8} In the emerging field of quantum engineering, SAWs find an opportunity thanks to their long coherence time.^{9–13} Recently, SAWs are also attracting renewed attention in the field of spintronics, where the ability for transferring their angular momenta to spins could be exploited.^{14–19}

To expand the possibility of SAW devices, diagnosing spatiotemporal profile of the displacement field of SAWs would be beneficial. To this end, various optical measurement techniques are developed. The interferometric method observing the phase modulation due to surface

displacement,^{20–22} knife-edge method to observe the path modulation due to the surface tilt,²³ and the diffraction method utilizing the periodic nature of the displacement²⁴ are explored.

In this Letter, we show that the slope of the periodically tilting surface due to the coherently driven SAW can be sensitively measured with a polarimeter. One of the major motivations to explore the polarimetric measurement of SAWs is the fact that the small amount of polarization rotation can be precisely calibrated when polarimeters work in the shot-noise-limited regime. The polarimetric measurement may, thus, constitute a viable tool to quantitatively evaluate various SAW devices.

The experimental setup is schematically shown in Fig. 1(a). We analyze the signal in the three different settings labeled as (i)–(iii). They are aimed at detecting (i) the polarization modulation, (ii) the optical path modulations, and (iii) the background signal. In setting (i), the orthogonal polarization components of the reflected beam are split by a PBS, coupled separately to multi-mode fibers, and differentially measured by a balanced detector (Thorlabs: PDB465C). Here,

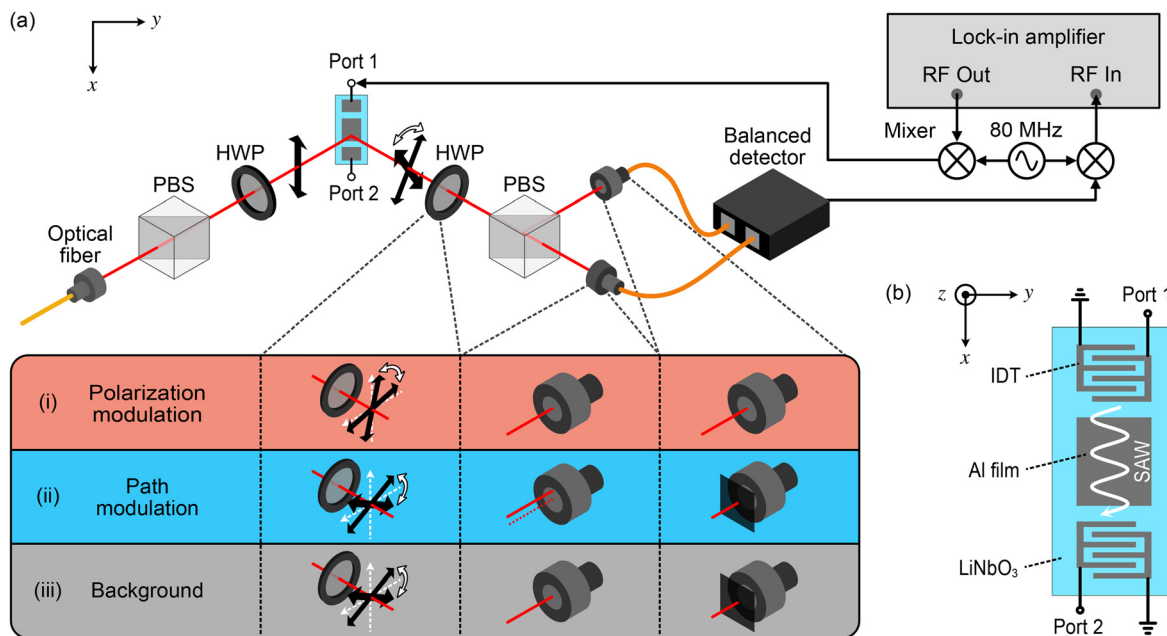


FIG. 1. Experimental setup and device for observing optical modulations induced by the SAW. (a) With a beam splitter (PBS) and a half-wave plate (HWP), the incident light is made linearly polarized with the polarization plane aligned parallel to the direction of SAW propagation (x -axis). The beam is focused with an objective lens (not shown) into a diameter of around $10\ \mu\text{m}$ on the device surface. The angle of incidence is set to 45° . The reflected beam is then collimated by another objective lens (not shown) and analyzed in the three different ways indicated as (i), (ii), and (iii) with HWP, PBS, and a balanced detector. The maximum power at the balanced detector is about $70\ \mu\text{W}$ for each input. (b) Schematic illustration of the SAW device with the coordinate system. The device consists of a YZ-cut LiNbO₃ substrate and aluminum interdigitated transducers (IDTs), which have 50 pairs of 1-mm-long fingers with $10\text{-}\mu\text{m}$ line and space. The two IDTs are separated by $812\ \mu\text{m}$, between which a 100-nm -thick Al film with the width of $1280\ \mu\text{m}$ and the length of $680\ \mu\text{m}$ is deposited.

the polarization plane is rotated with a HWP by the angle of 45° with respect to the original plane in order to maximize the amplitude of the polarization modulation and to eliminate the common-mode intensity fluctuations (see the [supplementary material](#)). Note that setting (i) is akin to the one employed to measure the longitudinal magneto-optical Kerr effect.²⁵ In setting (ii), the polarization plane is rotated by the angle of 90° with respect to the original plane so that one of the split beams has a negligible amplitude while the other maintains the original amplitude. The former beam is then blocked, and the latter beam alone is coupled into the multi-mode fiber with the beam deliberately misaligned along the x -axis with respect to the fiber, so that roughly half of the power is fed into the fiber. Setting (ii) is basically the same as the knife-edge method demonstrated before.²³ This setting is insensitive to the polarization modulation but highly sensitive to the deflection of the optical beam path along the x -axis (see the [supplementary material](#)). Setting (iii) is basically the same as setting (ii), but the beam is properly aligned so as to maximize the coupling into the fiber. The background signal (noise floor) measured by this setting is composed of the optical shot noise and the electrical noise of the measurement system.

Figure 1(b) shows the schematic of a SAW device under test. The SAW device is formed by an Al film on a LiNbO₃ substrate. The SAW is excited and detected through interdigitated transducers (IDTs), which convert the radio frequency (rf) signal to the SAW signal and vice versa. The SAW with a wavelength of $\sim 40\ \mu\text{m}$ is generated by driving the IDT of port 1 with an rf signal at the frequency of

$\omega_{\text{SAW}}/2\pi \sim 86\ \text{MHz}$ and propagates along the x -direction, which is parallel to the crystalline z -axis of the LiNbO₃ substrate.

We first characterize the SAW propagation in the device. Figure 2(a) shows a transmission spectrum ($|S_{21}|$) of the SAW from port 1 to port 2 measured with a vector network analyzer. The peak around $86\ \text{MHz}$ corresponds to the center frequency of the band covered by the IDTs. The broad profile appears as a result of the dispersion of the SAW, where the IDTs select preferred wavelengths according to the geometry of the fingers. Small reflections by the IDTs result in the interference and appear as the fine structures in the spectrum. The maximum peak transmission around the center peak ($\sim -4\ \text{dB}$) indicates that the rf power loss is sufficiently low even in the presence of the Al film in between.

Figures 2(b) and 2(c), respectively, show spectra of the polarization modulations (red curves) and the path modulations (blue curves). Here, the result for the beam spot ($\sim 10\ \mu\text{m}$) placed at particular positions of the Al/LiNbO₃ region [bare LiNbO₃ region] of the device is shown in Fig. 2(b) [Fig. 2(c)]. For the measurements, the SAWs are driven from port 1 with an rf signal with the power of $-10\ \text{dBm}$ produced by mixing a fixed-frequency signal at $80\ \text{MHz}$ from an rf generator (Agilent: E8247C) and a variable-frequency signal at $5.5\text{--}6.5\ \text{MHz}$ from a lock-in amplifier (Zurich Instruments: HF2LI). The optical signal is acquired by the balanced detector shown in Fig. 1(a), mixed-down with the 80-MHz rf signal, and then demodulated with the lock-in amplifier. The spectra shown in Figs. 2(b) and 2(c) show an enhanced amplitude at around $86\ \text{MHz}$ similarly to the rf transmission

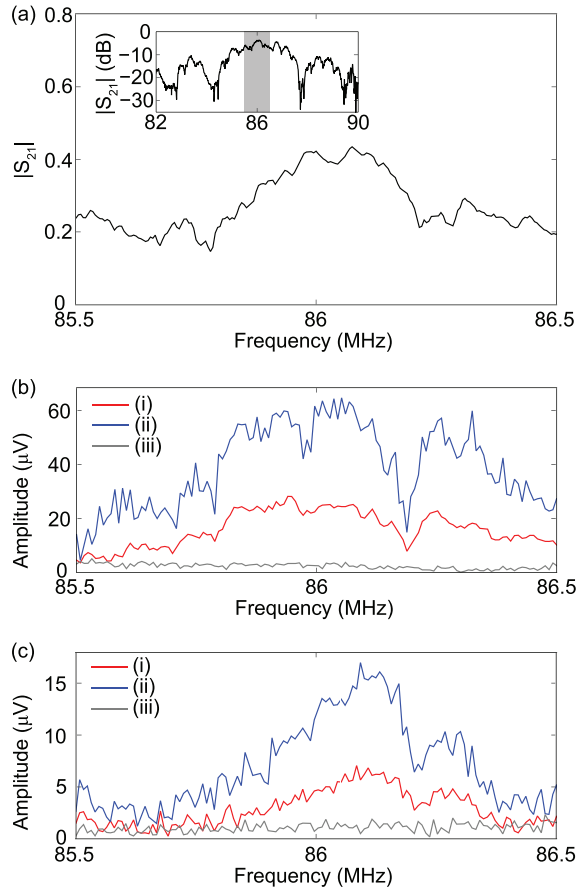


FIG. 2. Spectra of the SAW propagation, the optical path modulation, and the polarization modulation. (a) rf transmission spectrum from port 1 to port 2. The peak around 86 MHz corresponds to the center frequency of IDTs. The frequency range is the same as that in the following optical modulation spectroscopy. The inset shows the zoom-out of the frequency range in (a) indicated by the gray zone. (b) Spectra of the polarization modulation amplitude (red), the path modulation signal (blue), and the background signal (gray), each of which is acquired in the corresponding setting denoted as (i)–(iii) in Fig. 1(a). The data are taken in the Al/LiNbO₃ region. (c) Spectra taken in the bare LiNbO₃ region.

spectrum shown in Fig. 2(a). Note that the spectra of the modulated optical signals contain the local information of the SAW and, thus, sensitive to the interference effects of the SAW. There is no noticeable structure in the spectra of the background signal (gray curves). We confirm that there is no stray rf field directly coupled to the balanced detector, little path modulation signal is found when the beam is properly aligned to maximally couple to the fiber, and little polarization modulation signal is found when the polarization plane of the reflected beam is rotated by the angle of 90° with respect to be the original plane. The spectra of the polarization modulations [red curves in Figs. 2(b) and 2(c)] constitute telltale evidence that the SAW can be measured with the polarimeter. Notably, the signal-to-noise ratio of the polarimetric method is comparable to that of the knife-edge method [blue curves in Figs. 2(b) and 2(c)].

To gain further insight, the spectra of the amplitude and the phase are acquired with respect to the drive frequency $\omega_{\text{SAW}}/2\pi$ while the position of the beam spot is scanned by 100 μm across the border between the Al/LiNbO₃ region and the bare LiNbO₃ region. Figures 3(a) and 3(b) show the spectra of the in-phase (real) component of the polarization modulation amplitude $\text{Re}[\alpha(x)]$ and that for the path modulation amplitudes $\text{Re}[L(x)]$ together with the respective cross sections at the frequency of 86 MHz and the phases $\phi(x)$ and $\phi'(x)$. Here, the polarization modulation amplitude $\alpha(x)$ is calibrated with the shot noise (see the supplementary material) and denoted in terms of rotation angle in units of radian. On the other hand, the amplitude $L(x)$ is not easily calibrated in units of meter and is, thus, denoted as the dimensionless value $\tilde{L}(x)$, which is normalized with respect to the optical power reflected off the surface position probed (see the supplementary material). These procedures enable us to make a fair comparison between the signals in the highly reflective Al/LiNbO₃ region and the modestly reflective bare LiNbO₃ region.

As shown in Figs. 3(a) and 3(b), the phases $\phi(x)$ and $\phi'(x)$ linearly develop as a function of the probe position x , i.e., $\phi(x) = q_{\text{Al}}x$ ($q_{\text{LN}}x$) and $\phi'(x) = q'_{\text{Al}}x$ ($q'_{\text{LN}}x$), in the Al/LiNbO₃ region (the bare LiNbO₃ region), respectively. Here, we obtain the wavelengths $\lambda_{\text{Al}} \equiv \frac{2\pi}{q_{\text{Al}}} = 40.3 \pm 0.6$ (32.7 ± 4.0) μm in the Al/LiNbO₃ region (the bare LiNbO₃ region) from the polarization modulation signal and $\lambda'_{\text{Al}} \equiv \frac{2\pi}{q'_{\text{Al}}} = 41.7 \pm 1.1$ (39.5 ± 0.5) μm in the Al/LiNbO₃ region (the bare LiNbO₃ region) from the path modulation signal. With separate experiments (see the supplementary material), we verify that the phases $\phi(x)$ and $\phi'(x)$ develop oppositely when the propagating direction of the SAW is switched. Assuming that the polarization-modulation amplitudes are uniform within the Al/LiNbO₃ region, we obtain $\alpha_{\text{Al}} = 2.91 \pm 0.09$ (2.82 ± 0.12) μrad by fitting the sinusoidal signal $\text{Re}[\alpha(x)]$ in the middle panel of Fig. 3(a) [Fig. S3(a)] with $\alpha_{\text{Al}} \cos(q_{\text{Al}}x)$, when the SAW propagates in the $+x$ ($-x$)-direction. Similar fitting with $\alpha_{\text{LN}} \cos(q_{\text{LN}}x)$ yields $\alpha_{\text{LN}} = 1.15 \pm 0.34$ (1.22 ± 0.17) μrad for the spot position x at the bare LiNbO₃ region.

The observed polarization and path modulations of the reflected light can be considered as the results of the moving boundary effect due to the SAW as illustrated in Fig. 4. Here, the boundary is the surface of the device having the normal vector $\mathbf{n}(x, t)$, which is periodically tilted with the slope angle denoted by $\theta_n(x, t) = \frac{\partial u_z(x, t)}{\partial x}$. Here, $u_z(x, t)$ is the z -component of the displacement field at position x and time t associated with the SAW. In the experimental configuration depicted in Fig. 1(a), the tilting surface with the slope $\theta_n(x, t)$ results in the polarization rotation in such a way as

$$\alpha(x, t) = \text{Re}[\alpha(x)e^{-i\omega_{\text{SAW}}t}] = \sqrt{2} \left(\frac{r_p}{r_s} - 1 \right) \theta_n(x, t), \quad (1)$$

where r_p and r_s are the Fresnel reflection coefficients for s-polarization and p-polarization, respectively (see the supplementary material). The amplitude of the path modulation $L(x, t)$ can also be expressed in terms of the slope angle as

$$L(x, t) = \text{Re}[L(x)e^{-i\omega_{\text{SAW}}t}] = 2l_0\theta_n(x, t), \quad (2)$$

where l_0 having the dimension of length is the proportional factor. It is then evident that the phases of $\text{Re}[\alpha(x)]$ and $\text{Re}[L(x)]$ may develop along x in the same way since both are dictated by $\theta_n(x, t)$. This is consistent with the observation shown in Fig. 3. In

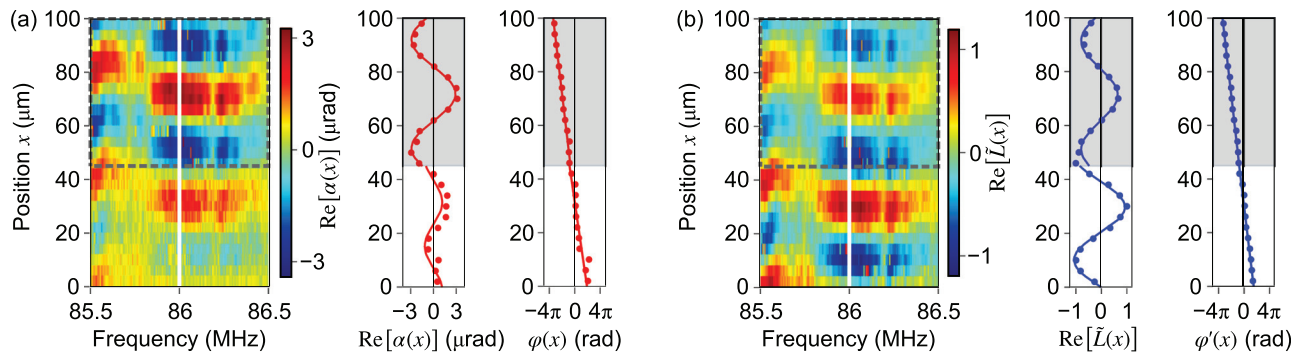


FIG. 3. Position dependence of the SAW-induced optical modulation signal spectra observed through the polarimetric method (a) and the knife-edge method (b). (a) Spectra of the polarization modulation $\text{Re}[\alpha(x)]$ acquired while the position of the beam spot x is scanned across the boundary between the Al/LiNbO₃ region (enclosed by the dashed gray rectangle) and the bare LiNbO₃ region. (b) Spectra of the normalized path modulation $\text{Re}[\tilde{L}(x)]$. Together with the color maps, cross sections at the frequency of 86 MHz (indicated by white lines in the color maps) and their associated phases are shown with fitting curves.

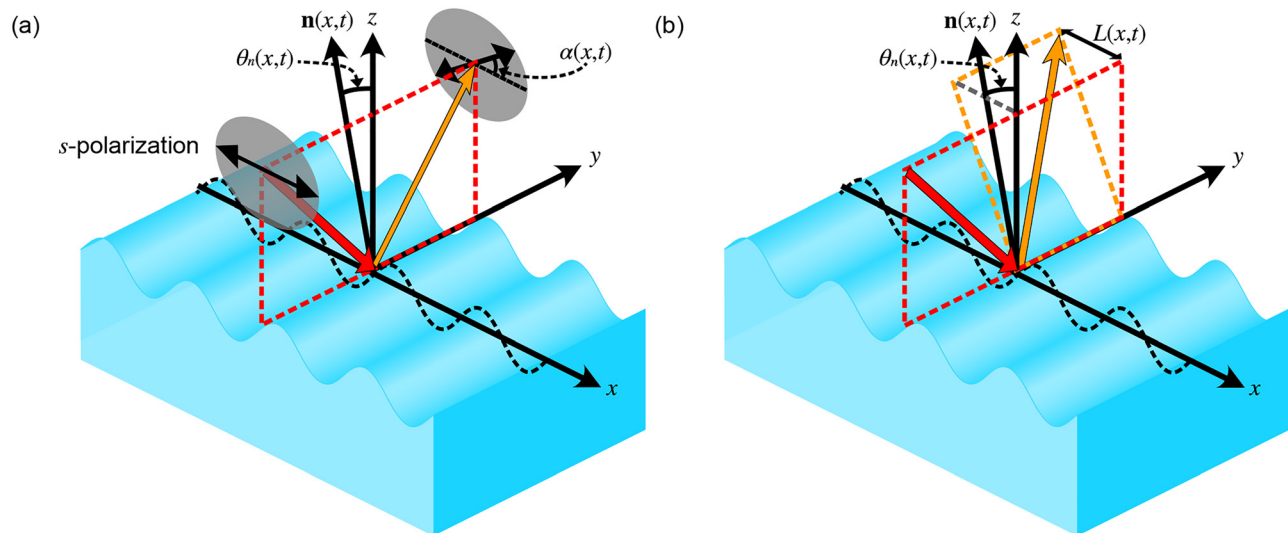


FIG. 4. Schematic illustrations of (a) the polarization modulation and (b) the path modulation. Variables $\mathbf{n}(x, t)$, $\theta_n(x, t)$, $\alpha(x, t)$, and $L(x, t)$ represent the normal vector of the surface at the light spot, the slope angle of the surface, the angle of the polarization rotation, and the departure of the reflected light from the nominal position, respectively.

separate experiments (see the [supplementary material](#)), we also confirm that the modulation amplitudes both depend linearly on the amplitude of the slope $\theta_n(x, t)$ and, thus, z -component of the displacement field $u_z(x, t)$ (which is proportional to the square root of the rf power used for driving the SAW). These facts support the model in which the polarization modulation is directly linked to the slope angle $\theta_n(x, t)$.

One of the most appealing features of the polarimetric measurement is the fact that the amount of polarization rotation can be precisely calibrated with shot noise when working in the shot-noise-limited regime (see the [supplementary material](#)). Given the polarization rotation angle, the slope angle $\theta_n(x)$ can be estimated from Eq. (1). We have $\theta_{n,\text{Al}} = 1.04 \pm 0.03$ (1.00 ± 0.04) μrad for x in the Al/LiNbO₃ region and $\theta_{n,\text{LN}} = 0.54 \pm 0.16$ (0.58 ± 0.08) μrad for x in the bare LiNbO₃ region, when the SAW propagates in the $+x$ ($-x$) direction, which are in reasonable agreement with the value $|\theta_n(x)|$

$\sim 1.8 \mu\text{rad}$ separately estimated from the physical dimension of the device and the driving power (see the [supplementary material](#)). There is a discrepancy between $\theta_{n,\text{Al}}$ and $\theta_{n,\text{LN}}$, though. The discrepancy may be caused by the difference between the amplitudes of the displacement $|u_z(x)|$ in the Al/LiNbO₃ region and that in the LiNbO₃ region due to, e.g., extra reflection at the boundary between the Al/LiNbO₃ region and the bare LiNbO₃ region, and the resultant interference effect. Other possibilities may be due to the optoelastic effect or the optical uniaxial anisotropy of the LiNbO₃ single crystal.

Finally, we note that, from the calibrated polarization-modulation amplitude, we can negate another mechanism that might cause polarization rotation, namely, the magneto-optical Kerr effect. The Kerr effect here could be caused by the effective magnetic field created by the SAW-induced vortex field.^{14–17} As discussed in the [supplementary material](#), the expected Kerr rotation is too small to account for the observed polarization rotation.

In summary, we demonstrated the polarimetric measurement of SAWs. The signal-to-noise ratio of the polarimetric method is on par with that of the knife-edge method. The precisely calibrated polarimetric measurement can be a viable tool to quantitatively evaluate the spatiotemporal profile of the displacement field of SAWs.

See the [supplementary material](#) for details on the theoretical models of the polarization and path modulations, measurement settings, SAW direction dependence, sanity check of the models with experiments, calibration of the measured modulation signals, estimate of the amplitude of the surface slope angle, and magneto-optical Kerr rotation due to the Barnett field.

We are indebted to Rekishu Yamazaki, Atsushi Noguchi, Yosuke Nakata, Maria Fuwa, and Shotaro Kano for useful discussion. We acknowledge financial support from JST ERATO (Grant No. JPMJER1601), JSPS KAKENHI (Grant No. JP20K15162), JST PRESTO (Grant No. JPMJPR200A), and the Collaborative Research Program of the Institute for Chemical Research, Kyoto University.

AUTHOR DECLARATIONS

Conflict of Interest

The authors have no conflicts to disclose.

Author Contributions

K.T., R.H., T.O., and K.U. conceived the experiment. K.T. and R.H. built the experimental setup, fabricated the SAW device, and performed the measurements. K.T., R.H., Y.O., R.S., and K.U. analyzed the data and developed the phenomenological model. With the inputs from Y.O., T.O., and Y.N., K.T., R.H., and K.U. wrote the manuscript. T.O., Y.N., and K.U. provided general research supervision. K.T. and R.H. contributed equally to this work.

DATA AVAILABILITY

The data that support the findings of this study are available from the corresponding authors upon reasonable request.

REFERENCES

- ¹L. D. Landau and E. M. Lifshitz, *Theory of Elasticity*, 3rd ed. (Butterworth-Heinemann, Oxford, 1986).
- ²K. S. Thorne and R. D. Blandford, *Modern Classical Physics* (Princeton University Press, Princeton, 2017).
- ³C. C. W. Ruppel, "Acoustic wave filter technology—A review," *IEEE Trans. Ultrasonics, Ferroelectr., Frequency Control* **64**, 1390–1400 (2017).
- ⁴F. Z. Bi and B. P. Barber, "Bulk acoustic wave RF technology," *IEEE Microwave Mag.* **9**, 65–80 (2008).
- ⁵C. Campbell, *Surface Acoustic Wave Devices for Mobile and Wireless Communications* (Academic Press, 1998).
- ⁶K. Lange, B. E. Rapp, and M. Rapp, "Surface acoustic wave biosensors: A review," *Anal. Bioanal. Chem.* **391**, 1509–1519 (2008).
- ⁷M. Rocha-Gaso, C. March-Iborra, A. Montoya-Baides, and A. Arnau-Vives, "Surface generated acoustic wave biosensors for the detection of pathogens: A review," *Sensors* **9**, 5740–5769 (2009).
- ⁸S. I. Zida, Y. D. Lin, and Y. L. Khung, "Current trends on surface acoustic wave biosensors," *Adv. Mater. Technol.* **6**, 2001018 (2021).
- ⁹M. J. A. Schuetz, E. M. Kessler, G. Giedke, L. M. K. Vandersypen, M. D. Lukin, and J. I. Cirac, "Universal quantum transducers based on surface acoustic waves," *Phys. Rev. X* **5**, 031031 (2015).
- ¹⁰B. A. Moores, L. R. Sletten, J. J. Viennot, and K. W. Lehnert, "Cavity quantum acoustic device in the multimode strong coupling regime," *Phys. Rev. Lett.* **120**, 227701 (2018).
- ¹¹K. J. Satzinger, Y. P. Zhong, H.-S. Chang, G. A. Peairs, A. Bienfait, M.-H. Chou, A. Y. Cleland, C. R. Conner, . Dumur, J. Grebel, I. Gutierrez, B. H. November, R. G. Povey, S. J. Whiteley, D. D. Awschalom, D. I. Schuster, and A. N. Cleland, "Quantum control of surface acoustic-wave phonons," *Nature* **563**, 661–665 (2018).
- ¹²A. Noguchi, R. Yamazaki, Y. Tabuchi, and Y. Nakamura, "Single-photon quantum regime of artificial radiation pressure on a surface acoustic wave resonator," *Nat. Commun.* **11**, 1183 (2020).
- ¹³R. Manenti, A. F. Kockum, A. Patterson, T. Behrle, J. Rahamim, G. Tancredi, F. Nori, and P. J. Leek, "Circuit quantum acoustodynamics with surface acoustic waves," *Nat. Commun.* **8**, 975 (2017).
- ¹⁴M. Matsuo, J. Ieda, K. Harii, E. Saitoh, and S. Maekawa, "Mechanical generation of spin current by spin-rotation coupling," *Phys. Rev. B* **87**, 180402 (2013).
- ¹⁵J. Ieda, M. Matsuo, and S. Maekawa, "Theory of mechanical spin current generation via spin-rotation coupling," *Solid State Commun.* **198**, 52–58 (2014).
- ¹⁶D. Kobayashi, T. Yoshikawa, M. Matsuo, R. Iguchi, S. Maekawa, E. Saitoh, and Y. Nozaki, "Spin current generation using a surface acoustic wave generated via spin-rotation coupling," *Phys. Rev. Lett.* **119**, 077202 (2017).
- ¹⁷Y. Kurimune, M. Matsuo, and Y. Nozaki, "Observation of gyromagnetic spin wave resonance in NiFe films," *Phys. Rev. Lett.* **124**, 217205 (2020).
- ¹⁸D. A. Bozhko, V. I. Vasyuchka, A. V. Chumak, and A. A. Serga, "Magnon-phonon interactions in magnon spintronics," *Low Temp. Phys.* **46**, 383–399 (2020).
- ¹⁹M. Weiler, H. Huebl, F. S. Goerg, F. D. Czeschka, R. Gross, and S. T. B. Gonnenwein, "Spin pumping with coherent elastic waves," *Phys. Rev. Lett.* **108**, 176601 (2012).
- ²⁰K. A. Hashimoto, "Laser probe based on a sagnac interferometer with fast mechanical scan for RF surface and bulk acoustic wave devices," *IEEE Trans. Ultrasonics, Ferroelectr., Frequency Control* **58**, 187–194 (2011).
- ²¹J. V. Knuuttila, P. T. Tikka, and M. M. Salomaa, "Scanning Michelson interferometer for imaging surface acoustic wave fields," *Opt. Lett.* **25**, 613–615 (2000).
- ²²W. Fu, Z. Shen, Y. Xu, C.-H. Zou, R. Cheng, X. Han, and H. X. Tang, "Phononic integrated circuitry and spin-orbit interaction of phonons," *Nat. Commun.* **10**, 2743 (2019).
- ²³H. Kamizuma, L. Yang, T. Omori, K. Hashimoto, and M. Yamaguchi, "High-speed laser probing system for surface acoustic wave devices based on knife-edge method," *Jpn. J. Appl. Phys., Part 1* **44**, 4535 (2005).
- ²⁴R. J. Hallermeier and W. G. Mayer, "Light diffraction by ultrasonic surface waves of arbitrary standing-wave ratio," *J. Acoust. Soc. Am.* **47**, 1236–1240 (1970).
- ²⁵C.-Y. You and S.-C. Shin, "Derivation of simplified analytic formulae for magneto-optical Kerr effects," *Appl. Phys. Lett.* **69**, 1315–1317 (1996).